Engineering Structures 299 (2024) 117104

Contents lists available at ScienceDirect

Engineering Structures

journal homepage: www.elsevier.com/locate/engstruct

Numerical modelling of 3D concrete printing: material models, boundary conditions and failure identification

Dong An, Y.X. Zhang, Richard (Chunhui) Yang *

School of Engineering, Design and Built Environment, Western Sydney University, Penrith, NSW 2751, Australia

ARTICLE INFO

Keywords:
3D concrete printing (3DCP)
Three-dimensional (3-D)
Finite element (FE) model
3D printed concrete
Material model
Mechanical behaviour
Failure mode

ABSTRACT

3D concrete printing (3DCP) attracts significant attention as an innovative manufacturing technology for the construction industry. As one of the challenges in 3DCP, failure mechanisms of 3D printed concrete structures were not well understood yet and hard to predict. The three-dimensional finite element (FE) method is an effective method to simulate such a layer-by-layer process. However, some existing technical issues in FE modelling, including additional initial deformations, failure identification, selection of material models, concrete foundation interactions and initial imperfections, need to be addressed for accurate simulation of 3DCP. In this study, FE models using a novel tracing element approach are developed to capture mechanical behaviours and failure modes of typical 3D printed concrete structures. The developed FE models was validated by comparing the obtained numerical results with those data available in literature. Furthermore, four material constitutive models are investigated analytically and numerically to compare their applicability in modelling 3D printed concrete structures. The obtained results show that the Mohr-Coulomb and Concrete Damage Plasticity (CDP) models can accurately predict failure behaviours of 3D printed concrete structures.

1. Introduction

3DCP is a process of successive layer-by-layer extrusion of fresh concrete materials to build structures without having to use the formwork as in the traditional manufacturing of concrete structures. It has environmental and economic benefits when compared with traditional cast-in-place concrete processes. Furthermore, without using formwork, more freedoms in design can be acquired, along with accelerating the construction processes and saving on-site labour work [1–3]. Hence, in recent years, research on 3DCP technology for building up concrete structures has dramatically attracted a wide range of interests from both academia and engineers in the construction industry worldwide [4,5].

In the 3DCP process, the printed object must self-support from the moment of deposition onwards due to no formwork. This requires that 3D printed cementitious materials have a good enough 'buildability', which is their ability to keep geometrical stability subject to increasing gravitational loads during the layer-by-layer process [6]. Roussel [7] developed analytical models to predict the maximum printing height of a 3D printed product. The results suggested that satisfactory buildability for the 3D printed materials can be achieved via high yield stress and structuration rate. Le et al. [8] and Bong et al. [9] evaluated the buildability of 3D printable materials through qualitative buildability trials where regular cross-sectional columns were printed without noticeable deformations as high as possible. However, it remains very challenging to predict whether a product of 3DCP can be printed without excessive deformations and failures [10].

To determine the appropriate buildability of 3D printable materials, numerical modelling and simulations have been employed to simulate the 3DCP processes, which can avoid the expensive and time-consuming trial and test. Its prerequisite is to select a proper elastoplastic material model to characterise the early-age mechanical behaviour of concrete used in 3DCP. Di Carlo [11] utilized the Drucker–Prager yield criterion and time-dependent material properties to characterise the mechanical behaviours of concrete used in contour crafting, which was cured within 288 min after deposition. Xiao et al. [12] established a FE model by taking advantage of the CDP model and the traction-separation law to explore the effects of interfacial bond properties on the anisotropic mechanical behaviour of 3D printed concrete. Wolfs et al. [13] developed a numerical model to analyse the mechanical behaviour of fresh 3D printed concrete in the range of 0 to 90 min after material deposition. The model was based on a time-dependent Mohr-Coulomb failure criterion and linear stress–strain behaviour up to failure. After the research

* Corresponding author.
E-mail address: R.Yang@westernsydney.edu.au (R.(C. Yang).

https://doi.org/10.1016/j.engstruct.2023.117104

Available online 6 November 2023

reported in [13], the Mohr-Coulomb constitutive model was widely employed to characterise the plasticity of cementitious material in 3DCP because the parameters in the model are relatively simple to measure [14]. Despite this, only a few constitutive models were investigated, and a comprehensive understanding of the applicability of various constitutive models to 3D printed concrete is lacking.

To simulate the 3D concrete printing process and predict the failure height of 3D printed concrete structures accurately, Wolfs et al. [13] developed FE models based on their experimental work, where the model change function was employed to simulate the layer-by-layer 3D printing process. However, they ignored the influences of compressive behaviours of concrete specimens in material tests, leading to large discrepancies between numerical and experimental results. Jayathilakage et al. [15] experimentally investigated the failures of 3D printed concrete structures and developed a finite difference model (FDM) to simulate the process. They proposed a buildability criterion with high accuracy, but it may not be suitable for lower aspect ratios existing in 3DCP layer geometries. On top of the numerical work from Wolfs et al. [13,16], Ooms et al. [17] devised a parametric modelling strategy to simulate the 3DCP process. The technical issue of additional initial deformation caused by tie constraint was pointed out (more details can be found in Section 2.5). To solve this problem, the contacted-based interaction, instead of the tie constraint, was used to simulate the inter-layer contact condition. However, damping was introduced in the implicit analysis, decreasing the reliability of the FE model. Recently, Liu and Sun [18] devised a numerical model to predict the buckling failure of a 3DCP cylinder, where the interfacial area was proposed to simulate the cross-section shape of the printed layer. However, their FE model required enormous computing resources due to its complexity. Moreover, the modelling methods of concrete foundation interactions and initial imperfections, as well as identifying failures of 3D printed concrete structures, were various and even vague in existing limited studies [13,15–19]. Related optimal modelling methods and their underlying mechanisms have yet to be deeply investigated [20,21]. Hence, a comprehensive understanding of the modelling of 3DCP needs to be improved, and numerical methods need to be developed to accurately simulate the 3DCP process and capture the mechanical behaviours of the 3D printed concrete. Specifically, in this research, a new tracing element approach will be devised to mitigate the unwanted additional initial deformations in 3DCP's FE modelling to improve accuracy.

This study aims to sort out main technical issues in FE modelling and simulations of 3DCP, including additional initial deformations, failure identification, selection of material models, concrete foundation interactions and initial imperfections. 3D FE models are devised to accurately simulate the layer-by-layer 3DCP processes considering various material properties and boundary conditions. The tracing element approach is developed to mitigate the influences of initial deformations. The developed models are further used to investigate the failure mechanisms and behaviours of typical 3D printed concrete structures. Four 3D printed concrete structures are selected to investigate numerically to demonstrate the effectiveness of the devised 3-D FE models. The numerical results are compared with those reported in literature to validate those models. Four constitutive models are investigated analytically and numerically to compare their applicability in characterising mechanical behaviours of fresh concrete used in 3DCP.

This paper is structured with five sections. Section 2 introduces the FE modelling of 3DCP using the tracing element approach. Section 3 conducts the FE analysis based on the FE modelling of four typical 3D printed concrete structures, including validation of models, failure analysis and identification, the effectiveness analysis of the proposed tracing element approach, and investigating the influence of bottom boundary conditions. Section 4 carries out the theoretical study of various constitutive models used to characterise the early-age mechanical behaviours of 3D printed concrete. Section 5 draws conclusions, lists the limitation of the current modelling method, and makes recommendations for future work.

2. FE modelling using novel tracing element approach

In this study, a series of 3D FE models were developed to simulate layer-by-layer 3DCP processes using the novel tracing element approach. To improve the accuracy of the simulation of 3DCP, five key aspects, including additional initial deformations, identification of failure, selection of material models, concrete foundation interactions, and initial imperfections in 3D FE models were carefully considered. The 3D FEA process and methodology using the tracing element approach are depicted in Fig. 1, where those five aspects mentioned above are underlined. The 3D FEA process includes three steps: a) pre-processing (preparation); b) processing (solution); and c) post-processing (analysis). The pre-processing step includes defining geometric models, material models and boundary conditions. The processing step is to solve equilibrium equations based on adding elements for simulating layer-by-layer 3DCP processes. In the post-processing step, the failures of 3D printed concrete structures can be identified and their mechanical behaviours can be captured accurately.

2.1. Geometric models

In pre-processing step, the 3D printed object is built as a 'part' according to its geometry. By 'partition', the part is divided into slices, which are used to simulate printed layers or their portions – segments. To precisely simulate the 3D printing process, the FE model was developed using a segment-by-segment addition process using the well-known element birth and death technology, in which the elements are added into the simulation process set by set. Every layer of 3D printed object is divided into four segments to balance simulation accuracy and computational cost [17]. When virtual printing starts, the 3D printed object is removed using the model change function available in Abaqus/Standard [22]. Then each segment is added in a single step following the printing sequence along a pre-defined print path.

2.2. Material models

Table 1 lists the values of crucial material parameters of 3D printed concrete. To formulate the elastoplastic behaviours of the concrete materials, the Mohr-Coulomb criterion [23] was commonly adopted [13,15–18], which is

$$\tau_y = C(t) + \sigma_n \bullet \tan\varphi \tag{1}$$

where, $C(t)$ is the cohesion yield stress between particles bonded by cement, and φ is the internal friction angle caused by the frictional resistance and interlocking between internal particles. The shear yield stress and acting normal stress are given by τ_y and σ_n, respectively.

To characterise the elastic behaviours of concrete before failure, the Young's modulus $E(t)$ and Poisson ratio ν are employed. It's important to note that time-dependent material models for Young's modulus $E(t)$ and cohesion yield stress $C(t)$ were adopted to describe the thixotropic behaviours of concrete, where t denotes the time elapsed after extrusion. The thixotropy of cementitious materials enables the strength and stiffness to increase over time, with the rate of increase known as the "structuration rate," dependent on material compositions. In this model, each printed segment is characterised by an amplitude function using a field variable to simulate the material evolution in the 3D printing process. In addition, three other constitutive models, including the von Mises model, Drucker-Prager model, and CDP model, are investigated in Section 4 to compare their applicability in characterising the early-age mechanical behaviours of 3D printed cementitious materials.

2.3. Boundary conditions

The fixed bottom and contact-based interaction are commonly used to define the boundary condition between the print bed and the first

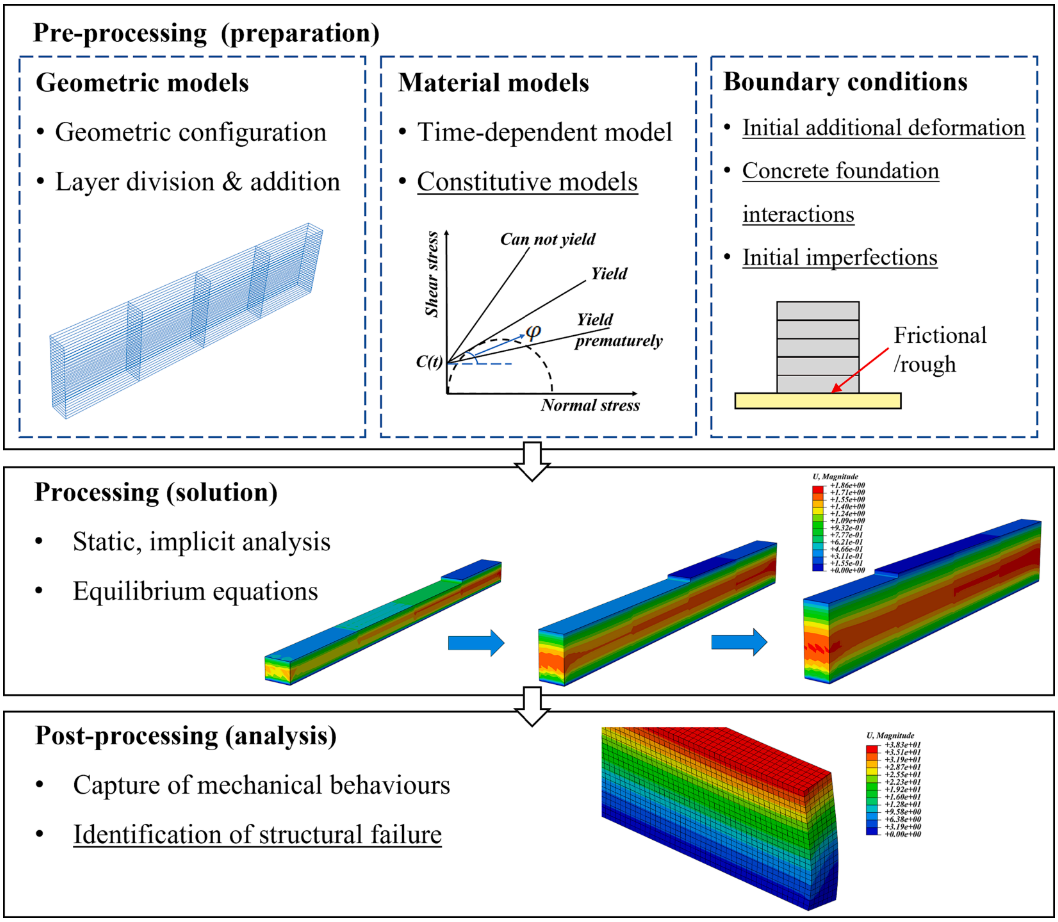

Fig. 1. FE Model methodology on 3DCP using tracing element approach.

Table 1
Crucial material parameters of the time-dependent concrete materials [13,15,16].

Model name	*E(t)* (kPa)	*ν*	*C(t)* (kPa)	*φ* (°)	*Ψ* (°)
Wall 1 and Wall 2	$1.705t + 39.48$	0.3	$0.0636t + 2.6$	3	13
Ring 1	$1.2t + 77.9$	0.3	$0.058t + 3.05$	20	13
Ring 2	$7.4t + 51.6$	0.3	$0.002t + 0.3$	42	0.7

layer [17,18,20]. In the latter case, the normal behaviour is defined as 'hard' contact and the tangential behaviour can be defined as rough or penalty with a friction coefficient. Slip in the first concrete layer was observed in [13], suggesting that the contact-based interaction might be more suitable for 3DCP simulation.

Initial imperfections are artificially introduced to simulate the geometric nonlinearity of actual 3D printed structures. Specifically, a bifurcation analysis of the 3D printed object is performed to derive its buckling modes. By editing the "imperfection" keyword available in Abaqus/Standard [22], the first buckling mode is typically integrated into the model to serve as the initial imperfection profile, and a small imperfection amplitude, such as 0.1 %, can be applied.

2.4. Processing

The choice of analysis type depends on the underlying assumptions. For simulating the printing process with tie constraints (or the common node technology) applied, static, implicit analysis is employed. In this scenario, automatic stabilization with default settings is used, eliminating the need for significant numerical damping present in dynamic implicit analysis [17]. The numerical equation of equilibrium is

$$K \times \Delta D = \Delta F \tag{2}$$

where, K is the material stiffness matrix, dependent on the material properties, ΔD is the incremental displacement based on boundary conditions of printing system, and ΔF is the incremental loading based on existing element force.

However, if the tie constraint is simply used, the bottom of the added segment would suffer additional initial deformations, decreasing the accuracy of incremental displacement ΔD, as shown in Fig. 2. More specifically, when the new segment is added, its bottom nodes would be pulled down towards the deformed model due to the common node technology. In contrast, its top nodes would be activated in the undeformed position of the predefined print path. As a result, the bottom elements would be severely distorted and suffer additional initial deformations. In such a case, the stress state of 3D printed concrete cannot be accurately predicted, whether the reactive type is activating with strain or strain-free [13,16,17].

Essentially, the issue of additional initial deformation is involved with boundary conditions. Let $\widetilde{L_n}$ be the domain of the n^{th} concrete layer with the boundary $\partial\widetilde{L_n}$, as shown in Fig. 3 (a). In this case, when the n^{th} concrete layer is added to the model, the equation of equilibrium and boundary conditions are

$$\begin{cases} K \times \Delta D = \Delta F in \widetilde{L_n} \\ \quad BCon \partial\widetilde{L_n} \end{cases} \tag{3}$$

where *BC* represents boundary conditions. In the y direction, *BC* should be

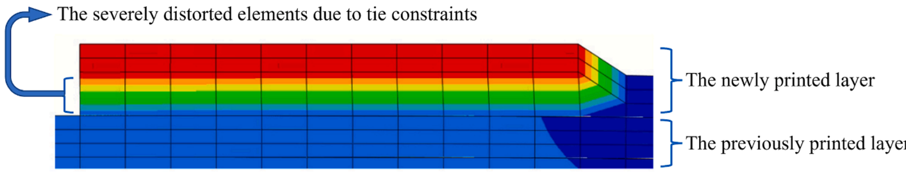

Fig. 2. The additional deformation of the newly printed layer [17].

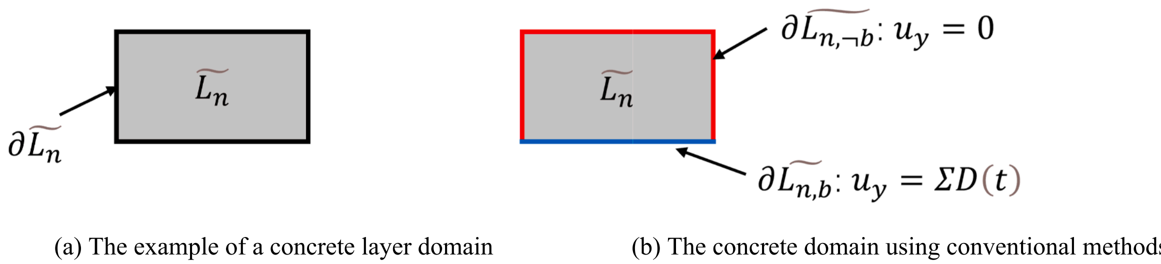

Fig. 3. Illustration of a domain of one concrete layer with its boundary.

$$u_y = \Sigma D(t) \tag{4}$$

where, u_y refers to the displacement boundary condition, and $\Sigma D(t)$ refers to the vertical accumulated compressive deformation of previously printed layers.

However, the displacement boundary conditions of the n^{th} concrete layer in the y direction in previous conventional methods simulating 3DCP (see Fig. 3 (b)) are

$$\begin{cases} u_y = \Sigma D(t) on \partial\widetilde{L_{n,b}} \\ u_y = 0 on \partial\widetilde{L_{n,\neg b}} \end{cases} \tag{5}$$

where $\partial\widetilde{L_{n,b}}$ refers to the bottom boundary and $\partial\widetilde{L_{n,\neg b}}$ refers to the boundary except the bottom. The $u_y = \Sigma D(t)$ on $\partial\widetilde{L_{n,b}}$ is caused by the tie constraint between the adjacent layers. The $u_y = 0$ on $\partial\widetilde{L_{n,\neg b}}$ is because the concrete layer $\widetilde{L_n}$ is added to its undeformed position of the predefined print path. The difference in boundary conditions leads to additional initial deformation.

2.5. Tracing element approach

The tracing element approach is developed to address the issue of the additional initial deformations. It allows the newly activated concrete segments to be added above the already-deformed printed concrete without additional initial deformations. The "tracing element" is the duplicated element for elements of the 3D printed object. By editing the keywords "Element copy" in the input file [22], tracing elements are created and share the same nodes with elements of 3D printed object but have different element numbers. Besides, the sole material property essential for tracing elements is an extremely low elastic modulus, e.g., 10^{-5} times of the initial Young's modulus *E(t)* ($t = 0$) of fresh concrete. This minimal stiffness ensures that the presence of these tracing elements has no impact on the calculation results of the original structure [24]. There is no need to define the density for those tracing elements, mitigating the influence of gravity. However, when modelling 3D printed concrete structures with complex geometries, such as a dome, the small Young's modulus may result in conditioning issues for stiffness matrices, leading to substantial alterations in stress distribution. Hence, the current tracing element approach is only a priori limited to structures with simple geometries, such as wall and ring structures.

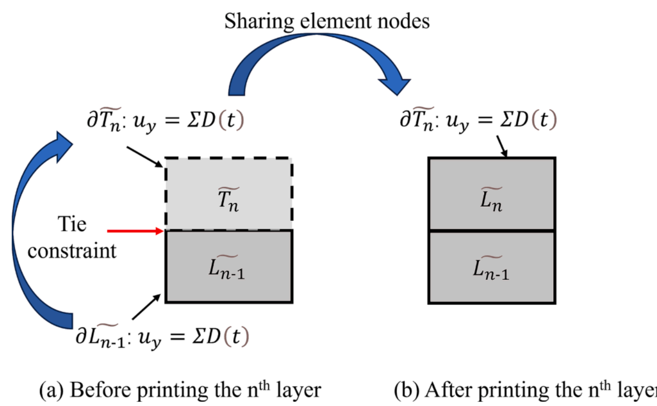

Fig. 4. The principle of the tracing element approach.

The proposed tracing element approach involves two steps: (a) before printing the concrete layer and (b) after printing the concrete layer, as shown in Fig. 4. At the end of the step of printing the (n-1)th layer $\widetilde{L_{n-1}}$, the displacement boundary conditions $\partial\widetilde{L_{n-1}}$ in y direction is $u_y = \Sigma D(t)$. For tracing element of the nth layer $\widetilde{T_n}$, it has the same displacement boundary condition in the y direction with $\widetilde{L_{n-1}}$ due to the tie constraint (or common node technology). When printing the nth concrete layer $\widetilde{L_n}$, $\widetilde{L_n}$ inherits the displacement boundary conditions of $\widetilde{T_n}$ as they share the element nodes.

Fig. 5 provides a comparison on the FE modelling with and without using the tracing element approach. As shown in Fig. 5 (b), there are three parts in a FE model of a 3D printed concrete structure: the tracing elements, the printed bed, and the concrete elements of the 3D printed structure. When the printing begins, all concrete elements are removed by model change, leaving the print bed and tracing elements. Then, the concrete elements are added to the model segment-by-segment and deformed under gravity. Meanwhile, the tracing elements move downwards with the already-added concrete elements. The newly added concrete elements would be activated at the position of responding tracing elements since the tracing elements and concrete elements share the same nodes. In such a case, the tracing elements prevent the

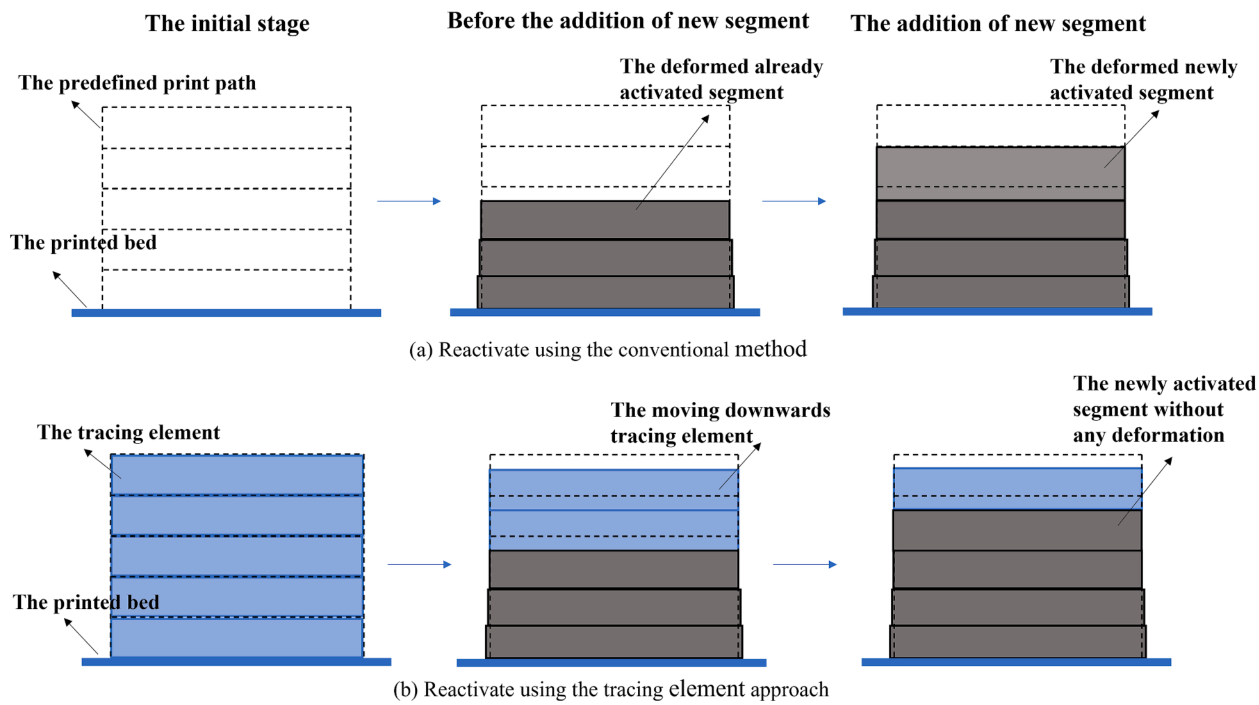

Fig. 5. The comparison between without and using the tracing element approach in simulations of 3DCP.

additional initial deformations and calibrate incremental displacements ΔD of concrete elements.

3. Finite element analysis of 3DCP

3.1. 3D printing of typical concrete structures

Four 3D printed concrete structures reported in literature, including two straight wall structures (namely Wall 1 and Wall 2) [16] and two ring structures (namely Ring 1 and Ring 2) [13,15], were selected as typical concrete structures to investigate the mechanical behaviours of 3D printed concrete structures and investigate the advantages of the presented modelling techniques. Their dimensions are given in Table 2.

Figs. 6, 7, and 8 show the pictures and 3-D FE models of Wall 1, Ring 1, and Ring 2 (the picture of Wall 2 was not shown in [16]). The FE models were developed using 8-node 3-D solid elements (C3D8), with a mesh size of 10 mm. The mesh size was determined through mesh sensitivity analyses, utilizing mesh sizes of 5, 10 and 15 mm. The results depicting strain energy with respect to the mesh size of Wall 1 are illustrated in Fig. 9 (a). It is evident that three mesh sizes exhibit comparable strain energy before and at the point of failure. A discrepancy emerges at the 24th layer, indicating the effects of mesh sizes on post-buckling behaviours. However, it is important to note that this variation does not compromise the efficacy of the proposed FE models in accurately capturing and identifying failure. Consequently, it can be concluded that the mesh size adopted in the manuscript is representative and suitable for the intended analysis.

Additionally, a sensitivity analysis was performed on the Young's modulus of the tracing elements to assess its impact on the modelling accuracy. Three different values, 10^{-4}, 10^{-5} and 10^{-6} times of the initial Young's modulus of fresh concrete, were employed for this analysis. The relationships between strain energy and printing layers are depicted in Fig. 9 (b). Notably, three curves corresponding to the different Young's modulus exhibit a high degree of overlap throughout the entire printing process, indicating the negligible effect of Young's modulus for tracing elements.

Table 2
The dimensions of 3D printed concrete structures.

Model	Length (mm)	Diameter (mm)	Width (mm)	Layer Height (mm)
Wall 1	1000	–	60	9.5
Wall 2	5000	–	60	9.5
Ring 1	–	500	40	10
Ring 2	–	320	40	10

3.2. Validations of FE models and discrepancy analysis

Using the FE modelling techniques mentioned earlier, the printing processes of four 3D printed structures were simulated. Table 3 shows their failure layers in experiments and numerical simulations from the current model and other researchers. The FE simulation results from the current model agree well with the experimental results. Fig. 10 (a)-(c) show the comparison between experimental and numerical results of the failure modes of Wall 1, Ring 1 and Ring 2. Evidently, the numerical model can capture the failure behaviours effectively, and the failure modes in the FE models are also in good agreement with the experimental results, such as the lateral collapse of Wall 1, buckling of Ring 1 and the extreme crush at the bottom of Ring 2. Specifically, regarding Ring 1, the maximum lateral displacement of printed ring structures occurred at the 12^{th}-13^{th} layer within a range of approximately 12–18 mm, and the maximum printed height reached approximately 270 mm by the 29^{th} layer [13]. In the proposed FE model of Ring 1, the predicted maximum lateral displacement is 13 mm on the 12^{th} layer, while the maximum printed height is 262,6 mm on the 28^{th} layer. (Detailed information for Ring 2, Wall 1, and Wall 2 was not provided in [15,16].) The harmonious concordance between the experimental and numerical results indicates that the developed FE model with the novel tracing element approach can simulate the 3DCP processes accurately.

The noticeable discrepancy among the predicted results of Ring 1 using various numerical methods can be observed in Table 4. Wolfs et al. [13] suggested that this discrepancy could be explained by the geometry being sensitive to imperfections and overestimating the material properties. To further investigate various modelling methods and find the optimal strategies, a comparison of the current model with FE models available in literature [13,17,18] is provided in Table.4. Two factors

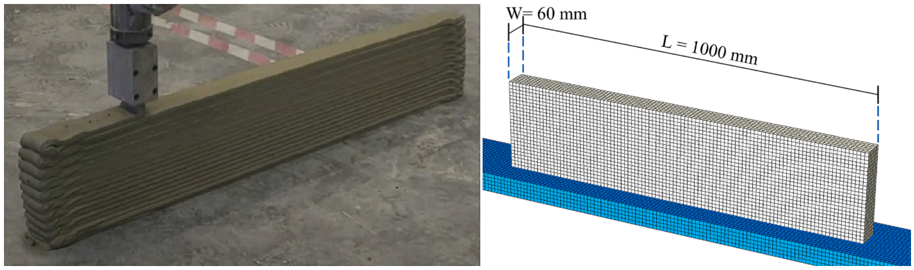

Fig. 6. The picture and FE model of Wall 1 [16].

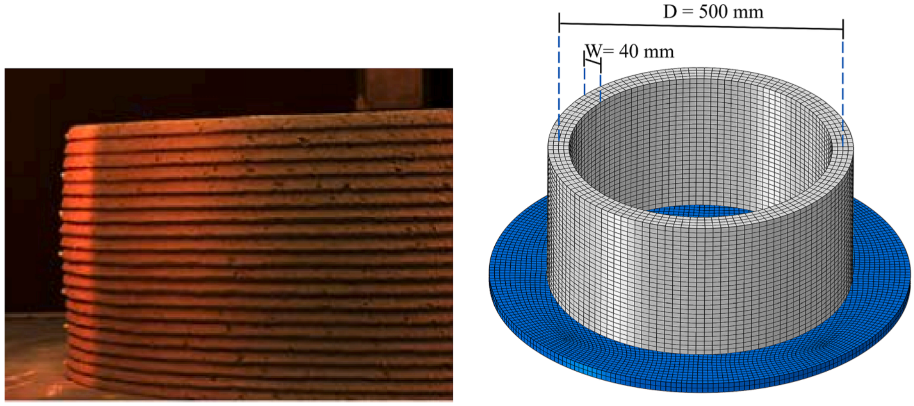

Fig. 7. The picture and FE model of Ring 1 [13].

Fig. 8. The picture and FE model of Ring 2 [15].

could be attributed to the disparity among different numerical predictions. The first one is the additional initial deformation. The current study mitigated it by the tracing element approach (see Sections 2.5 and 3.3).

Another reason is the identification of the failure. In practice, once the buckling initiates at the structure, it will collapse rapidly due to the second-order effect of the bending moment and its low stiffness. In the current study, the mutations of strains are employed to identify the failure. When the elastic buckling happens, the mutations of strains can be captured simultaneously (see Section 3.2). However, in [13,17], the failure was identified when (out of plane) deformations were equal to a predefined threshold. This means the printing process would only stop once a more considerable deformation occurs, even though the elastic buckling happens. Moreover, no artificial initial imperfection was defined in their model, further extending the buckling development and delaying the more considerable deformation.

3.3. Failure analysis and identification

The two typical failure modes of 3D printed concrete structures are elastic buckling and plastic collapse [14,25]. Fig. 11 (a)-(d) show mechanical states (including stresses and deformations) of four 3D printed concrete structures before and after failures with and without initial imperfection. It can be found that the failure modes of Wall 1, Wall 2 and Ring 1 are elastic buckling, while Ring 2 is plastic collapse.

Elastic buckling is defined as a loss of equilibrium of forces and moments, initiating uncontrolled deformations or displacements, whereas plastic collapse occurs when the material stress reaches the yield stress, resulting in plastic strain. Fig. 12 shows the plastic strain (PE) distribution of Ring 2 and Wall 2 when failures occur. No PE was found in Wall 2, although it collapsed laterally with a 38.3 mm displacement at the top, meaning the wall failed due to geometric nonlinearity. Conversely, a maximum PE of 3.2×10^{-4} is found in the bottom elements in Ring 2 without any structural buckling, which means the material nonlinearity contributes to the failure. Thus, the PE of concrete elements at failure time can be used in post-processing to identify failure modes of 3D printed structures.

Fig. 13 shows the development of von Mises stresses, logarithmic strains, and plastic strain of bottom elements in Wall 1 and Ring 2. It can be observed that the 3D printing process can be divided into the linear

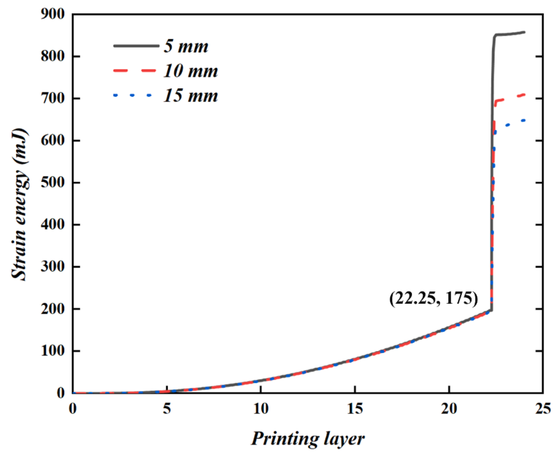

(a) The mesh sensitivity analysis

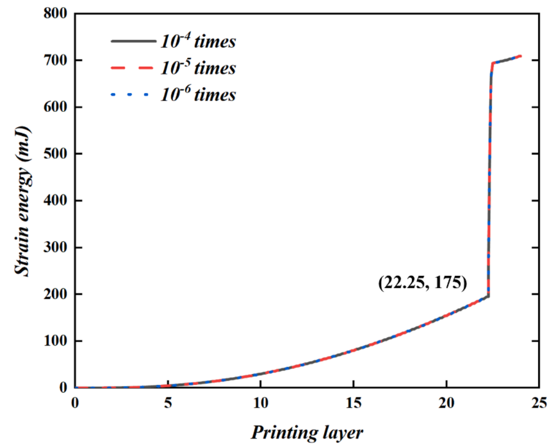

(b) The analysis on Young's modulus of tracing elements

Fig. 9. Strain energy sensitivity analyses.

Table 3
The failure layer derived by different methods.

	Wall 1	Wall 2	Ring 1	Ring 2
Experimental finding	21 and 22	27	29	10 and 11
Numerical prediction from current study	23	25	28	11
Numerical prediction from Wolfs *et al.* [13,16]	20	23	46	–
Numerical prediction from Jayathilakage *et al.* [15]	–	–	–	10
Numerical prediction from Ooms *et al.* [17]	22	–	48 and 49	–
Numerical prediction from Liu and Sun [18]	24	–	29	–

and failure stage, regardless of the failure mode. The linear phase refers to the period from the start of printing to the occurrence of failure. During the linear stage, the von Mises stresses and logarithmic strains of the bottom elements develop almost linearly, and no plastic strain generates. When printing the failure layer (the 23rd layer for Wall 1 and the 11th layer for Ring 2), stresses and logarithmic strains increase sharply, and the plastic strains are generated. Hence, the mutations of strains, including logarithmic and plastic strains, can be considered a critical index to identify the failure of 3D printed concrete structures for both elastic buckling and plastic collapse.

Introducing the initial imperfections can change the failure-deformation shapes of 3D printed concrete structures failing in elastic buckling. As shown in Fig. 11, when introducing the initial imperfections, the failure-deformation shapes of Wall 1, Wall 2, and Ring 1 changed from symmetrical vertical compression and lateral bulge to sizeable out-of-plane deformation, closer to the experimental phenomenon. However, no apparent change in the failure-deformation shape of Ring 2 can be observed since plastic collapse is not sensitive to the geometrical change - initial imperfections. Essentially, initial imperfections exist in actual structures and cause the *p*-δ effect during the loading stage, reducing the buckling strength of the structures.

3.4. Effectiveness analysis of the tracing element approach

The effectiveness of the tracing element approach in mitigating the effects of additional initial deformations is investigated in three aspects: avoiding the occurrence of additional initial deformations, the stress distribution when the structures fail and the predicted failure layer. Fig. 14 shows each layer thickness of Wall 1 when printing the 22nd and 23rd layers, which is the time just before the failure and the occurrence of the failure, respectively. It can be found that when printing the 22nd layer, initial deformations exist in the top 10 layers of Wall 1 using the traditional tie method: their thicknesses are much more than 9.5 mm, the original thickness of one layer. While using the tracing element approach, the thicknesses of printed layers are close to or less than 9.5 mm, which is closer to the reality that the printed layers are in compression due to the gravitational load from themselves and the newly printed layers. Similarly, when printing the 23rd layer, the additional initial deformations also happen in the top six layers of the model using the traditional tie method. While using the tracing element approach, each layer is thinner than 9.5 mm. Consequently, the tracing element approach can effectively avoid the appearance of initial deformation. It also can be observed that the thicknesses of the bottom layers of the model using the tracing element approach are more continuous, which matches reality more. It is meaningful to note that the influence of the initial deformation exists in each layer of FE models, but its influence on the bottom layers is covered up because they are subjected to more pressure from the upper layers.

The additional initial deformation would be pronounced when printing the failure layer because of the accumulation of the deformation of each layer and the instantaneous downward displacement at the time of failure. Fig. 15 shows the comparison of the deformation of Wall 1 by using the tracing element approach or not. In the case of the traditional method, the elements of the newly added layer are severely distorted, and their displacements are not continuous with previously printed layers due to the excessive initial deformation. While using the tracing element approach, no prominent distorted element can be observed, and the displacement field is more coordinated.

In predicting the failure layer, the advantage of using the tracing element approach is also evident. Table 5 shows the predicted failure layers of four 3D printed concrete structures using the tracing element approach or not. It can be found that the predicted layers using the tracing element approach are closer to the experimental results and almost higher than that of models using the traditional method. This is because the additional initial deformations mean increasing thicknesses of layers, and the accumulation of the increasing thicknesses of all layers causes a higher height of 3D printed concrete structures, leading to the underestimation of the predicted failure layer.

3.5. The influence of concrete foundation interactions

To investigate the influence of the concrete foundation interaction

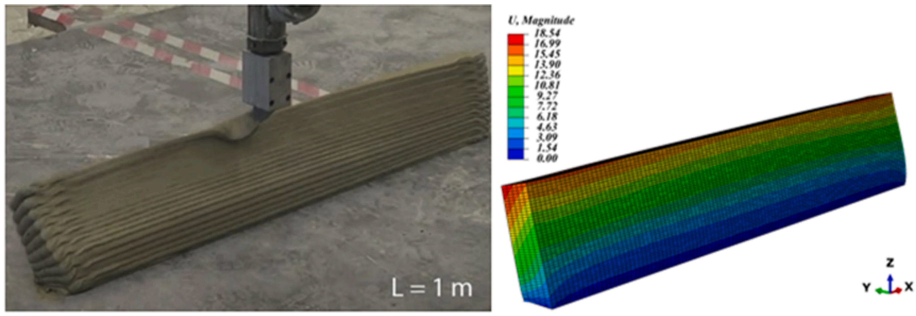

(a) The comparison between experimental and numerical results of Wall 1

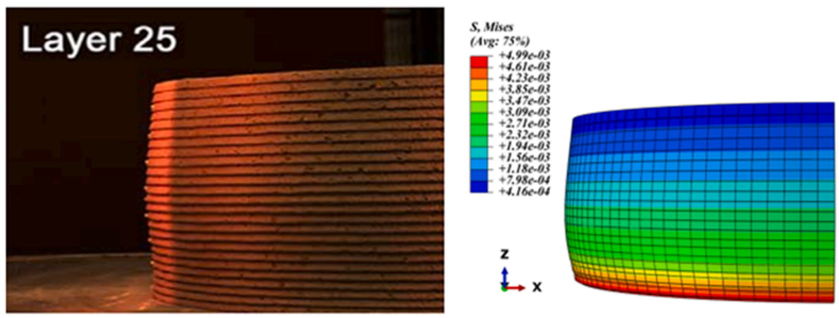

(b) The comparison between experimental and numerical results of Ring 1

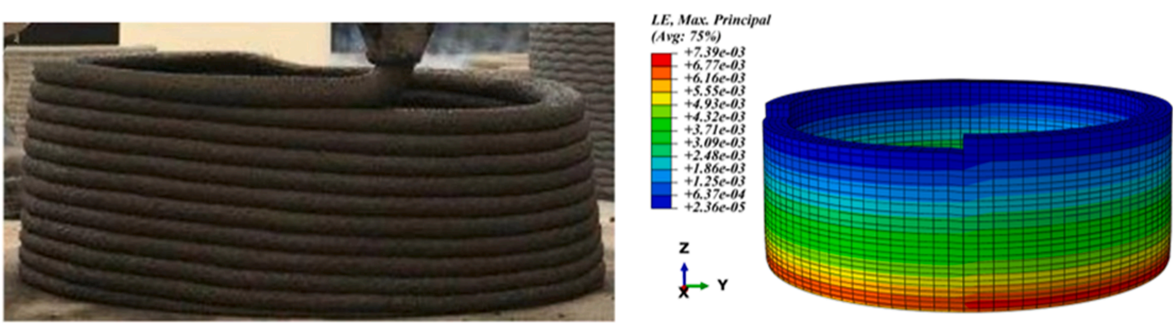

(c) The comparison between experimental and numerical results of Ring 2

Fig. 10. Comparisons between experimental and numerical results of deformations of 3D printed concrete structures.

Table 4
A comparison of the current model with FE models available in literature [13,17,18].

Model	Ring 1 in this study	Ring 1 in [13]	Ring 1 in [17]	Ring 1 in [18]
Predicted failure layer	28	46	48 / 49	29
Initial deformation	Removed by tracing element approach	Exist	Exist/ Removed by contact-based interaction	Removed by contact-based interaction
Identification of failure	Mutations of strains	Out of plane deformation	Deformation	Out of plane deformation
Initial imperfection	1 % of the width of the printed segment	No initial imperfection	An asymmetric loading	1 % of the width of the printed segment
Interaction of layers	Tie constraint	Tie constraint	Tie constraint/ Contact-based interaction	Contact-based interaction
Boundary condition	Rough contact	Fixed bottom in the axisymmetric FE model	Rough contact	Not mentioned in [18]

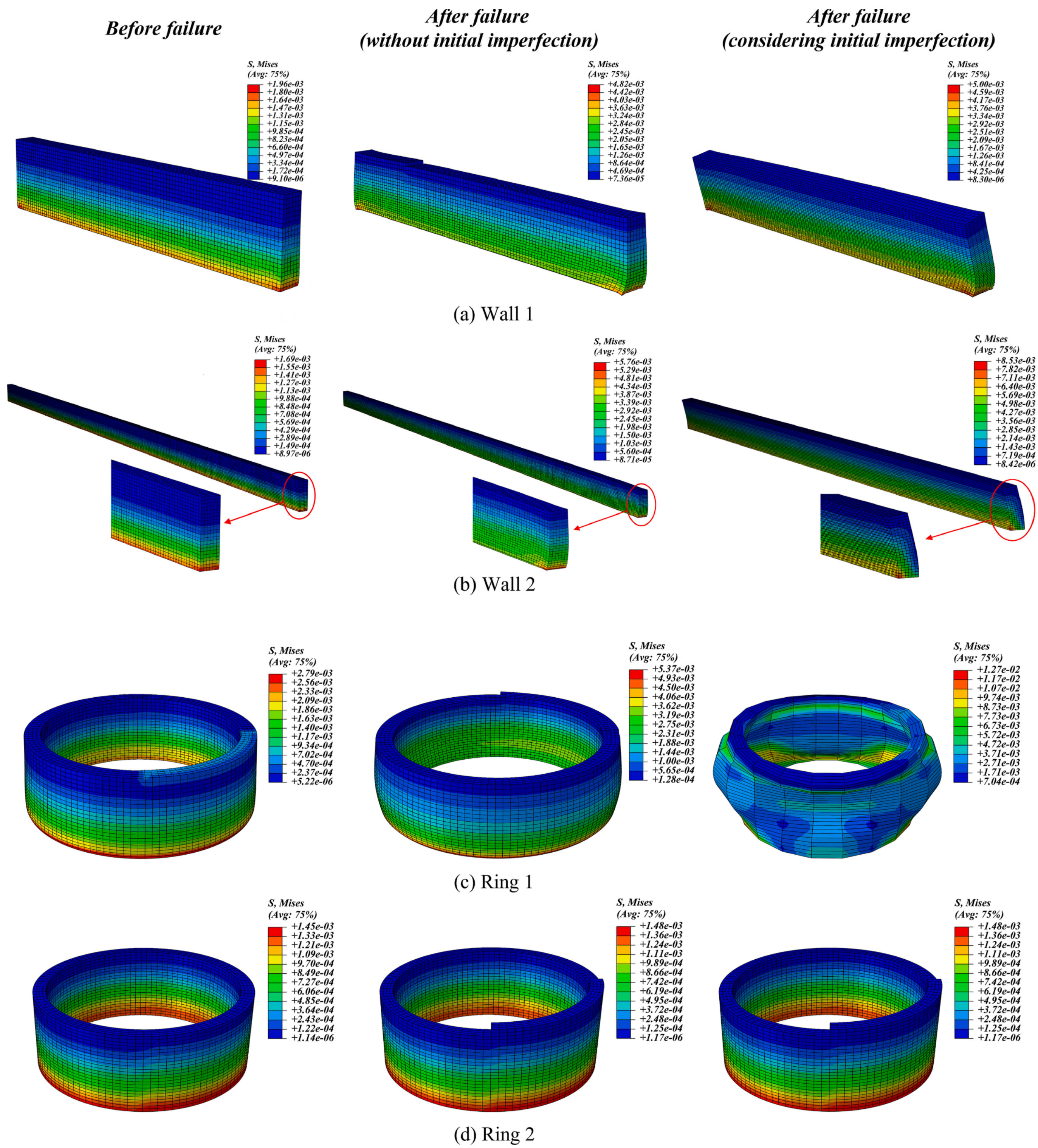

Fig. 11. Mechanical states of four 3D printed concrete structures before and after failure with and without initial imperfection.

on the failure behaviours of 3D printed concrete structures, three types of boundary conditions, including (a) a fixed bottom, (b) a frictional interaction with a friction coefficient of 0.6, and (c) a rough interaction with an infinite friction coefficient, are used in Wall 1 and Ring 2. The numerically predicted results are given in Table 6.

It can be found that the failure layer of Wall 1 is the 23rd layer regardless of boundary conditions. Moreover, Fig. 16 shows the maximum von Mises stresses and the average displacement amplitudes of corner nodes of Wall 1 using three boundary conditions. It can be found that there is a negative correlation between stress value and released displacement. The stress of the fixed bottom, 5.49 kPa, is about 11.7% higher than those of the other two conditions. In terms of displacement, no displacement could be observed in the fixed bottom, while a small number of displacements are found at the corners of the frictional and rough bottoms, reflecting the rheological behaviours of fresh concrete materials. The different constraint conditions of the bottom cause the difference in stress. Due to the displacement of the bottom layer restrained by the fixed boundary condition, stress cannot

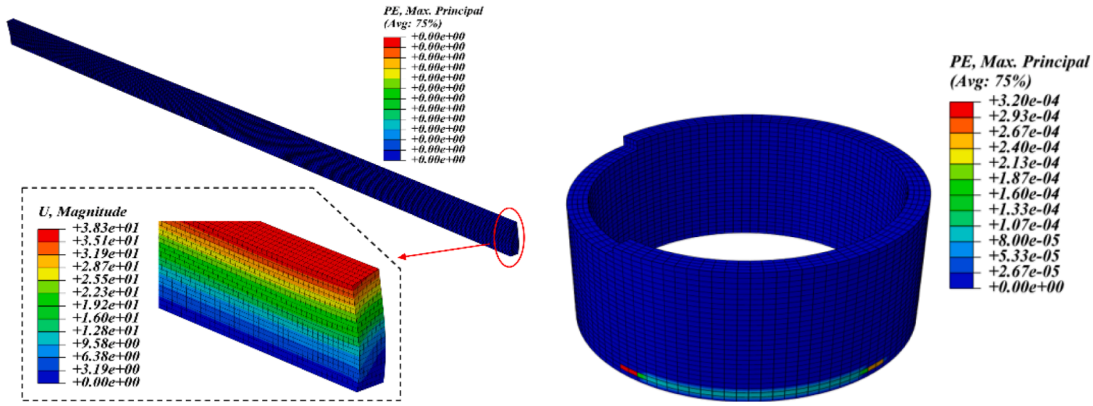

(a) Elastic buckling of Wall 2

(b)Plastic collapse of Ring 2

Fig. 12. Two failure modes of 3D printed concrete structures.

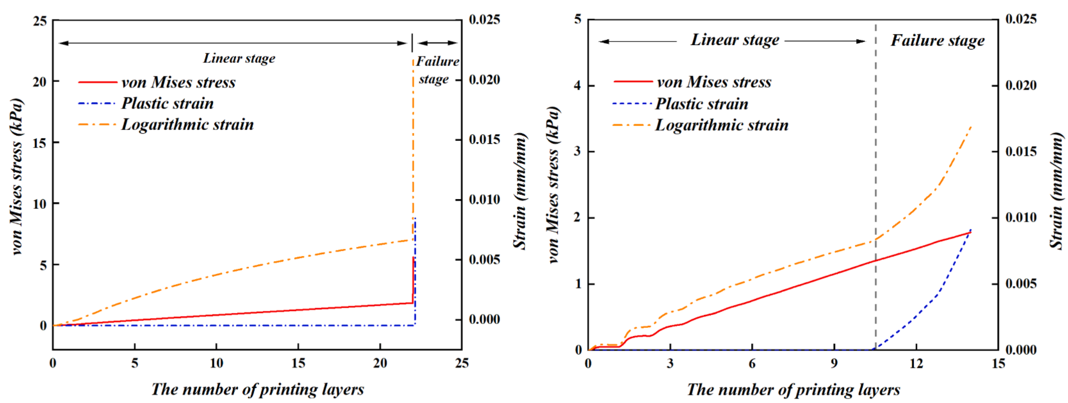

(a) The stress and strain variations of Wall 1

(b) The stress and strain variations of Ring 2

Fig. 13. The stress and strain variations of the bottom elements in 3D printed concrete structures.

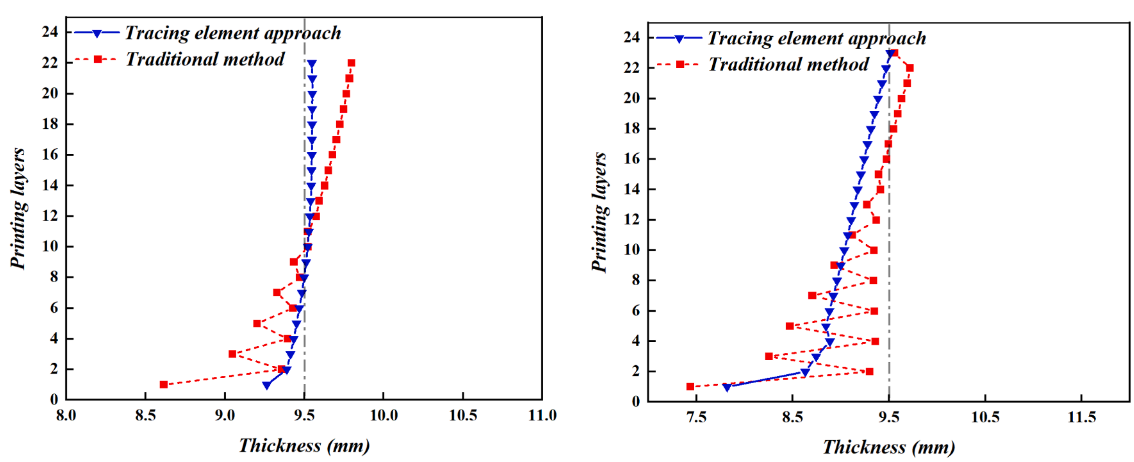

(a) The thickness profile when printing the 22nd layer

(b) The thickness profile when printing the 23rd layer

Fig. 14. The thicknesses of the printed layers before and after failure.

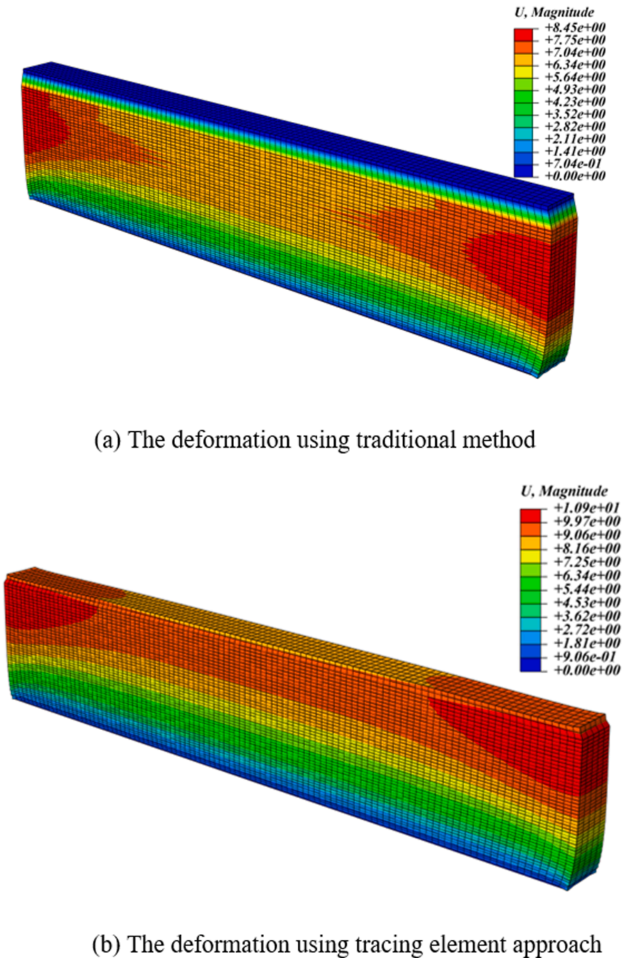

Fig. 15. The deformations of Wall 1 using different methods.

Table 5
The failure layers predicted by the FE models using different methods.

	Wall 1	Wall 2	Ring 1	Ring 2
Experiment	21 and 22	27	29	10 and 11
FE model using the tracing element approach	23	25	28	11
FE model using the traditional method	23	23	23	9

Table 6
The predicted failure layers of Wall 1 and Ring 2 using various boundary conditions.

Model	Boundary condition	Failure layer
Wall 1	(a) fixed	23
	(b) frictional	23
	(c) rough	23
Ring 2	(a) fixed	10
	(b) frictional	11
	(c) rough	11

be relieved, reaching the higher stress at the corner sooner.

For Ring 2, the negative correlation between stress value and released displacement was still valid. The failure layers of Ring 2 with the boundary conditions (a), (b) and (c) are the 10^{th}, 11^{th}, and 11^{th} layers, respectively. This is also because strongly constrained boundary condition leads to less displacement, higher stress, and lower failure height.

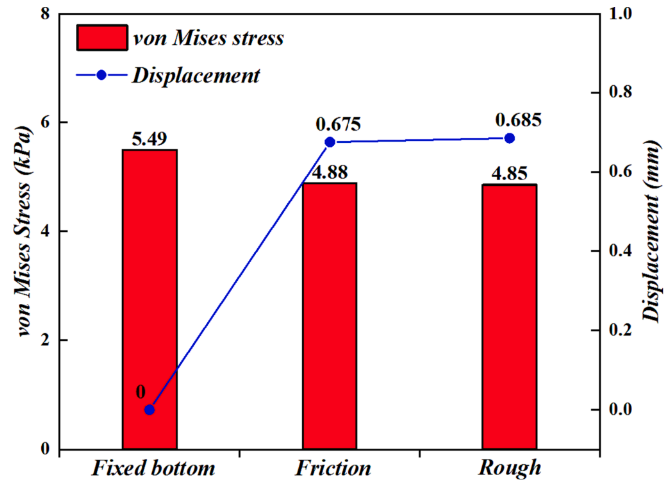

Fig. 16. The stress and the average displacement amplitude of corner nodes using various boundary conditions.

4. Comparative analysis of constitutive models

The choice of constitutive models depends mainly on the mechanical properties of the material, the stresses that the material is likely to experience in the application, and the experimental data available for calibration of the model parameters. Considering these factors and the relevant constitutive models used in previous studies, four constitutive models, including the von Mises model, Mohr-Coulomb model, Drucker-Prager model, and CDP model, are investigated numerically and analytically to compare their applicability in characterizing the early-age mechanical behaviours of 3D printed cementitious materials.

4.1. Theoretical comparison among four plastic constitutive models

von Mises model [21] is a classical model commonly used for ductile materials. The theory states that yielding occurs when the maximum distortion energy in a material is equal to the distortion energy at yielding in a uniaxial tensile test. It can be given as:

$$\sigma_v = \frac{1}{\sqrt{2}}\sqrt{(\sigma_1-\sigma_2)^2+(\sigma_2-\sigma_3)^2+(\sigma_3-\sigma_1)^2} \tag{6}$$

where, σ_v denotes the equivalent von Mises stress, σ_1, σ_2, σ_3 are the maximum, intermediate, and minimum principal stress, respectively.

Mohr-Coulomb criterion [22] is suitable for granular materials under monotonic loading, and it states that the material yields when the ratio of shear stress to normal stress at the shear plane reaches a maximum. It is given as Eq. (1).

Drucker-Prager model [26] is another pressure-dependent shear theory, and it can consider the influence of intermediate principal stress on the strength of materials compared with the Mohr-Coulomb criterion. The linear Drucker-Prager criterion can be written as:

$$F = t - p\tan\beta - d = 0 \tag{7}$$

where $t = \frac{1}{2}q\left[1+\frac{1}{K}-\left(1-\frac{1}{k}\right)\left(\frac{r}{q}\right)^3\right]$, is a type of deviatoric stress considering the influence of intermediate principal stress; β is the slope of the linear yield surface in the p-t stress plane and is commonly referred to as the friction angle of the material; d is the cohesion of the material; and K is the ratio of the yield stress in triaxial tension to the yield stress in triaxial compression and, thus, controls the dependence of the yield surface on the value of the intermediate principal stress.

CDP model [27] is a compressive model proposed for concrete material. The evolution of its yield surface is controlled by two hardening variables, compressive equivalent plastic strain $\widetilde{\varepsilon}_c^{pl}$ and tensile equivalent plastic strain $\widetilde{\varepsilon}_t^{pl}$. In terms of effective stresses, the yield function takes the form

$$F = \frac{1}{1-\alpha}\left(\overline{q} - 3\alpha\overline{p} + \beta\left(\widetilde{\varepsilon}^{pl}\right)\langle\widehat{\overline{\sigma}}_{max}\rangle - \gamma\langle-\widehat{\overline{\sigma}}_{max}\rangle\right) - \overline{\sigma}_c\left(\widetilde{\varepsilon}_c^{pl}\right) = 0 \quad (8)$$

where, α, β and γ are dimensionless constants; $\widehat{\overline{\sigma}}_{max}$ is the maximum principal effective stress and $\overline{\sigma}_c\left(\widetilde{\varepsilon}_c^{pl}\right)$ is the effective compressive cohesion stress, and it is defined as

$$\overline{\sigma}_c\left(\widetilde{\varepsilon}_c^{pl}\right) = E_0\left(\varepsilon_c - \widetilde{\varepsilon}_c^{pl}\right) \quad (9)$$

where, E_0 is the initial undamaged elastic stiffness of the material, and ε_c is the compressive strain.

To compare the four plastic models more clearly, the meridional plane (p, q) and the deviatoric plane (q, θ) are also employed to formulate their yield conditions, and the conversion relationship is:

$$p = \frac{1}{3}(\sigma_1 + \sigma_2 + \sigma_3) \quad (10)$$

$$q = \sqrt{\frac{(\sigma_1-\sigma_2)^2 + (\sigma_2-\sigma_3)^2 + (\sigma_3-\sigma_1)^2}{2}} \quad (11)$$

$$\cos\theta = (-2\sigma_1 + \sigma_2 + \sigma_3)/2q \quad (12)$$

where, p denotes the effective stress or mean stress, which can also be understood as hydrostatic pressure; q represents the deviatoric stress or shear stress, indicating the stress difference that leads to shear deformation; $\sigma_1 \geq \sigma_2 \geq \sigma_3$, and $0^\circ \leq \theta \leq 60^\circ$.

Their yield conditions can be summarised in Table 7 as follow:

where, σ_c is the compressive stress value, and ϕ is the internal friction angle of concrete materials.

During the 3D printing process, the 3D printed concrete is subjected to the gravitational load, and its mechanical state is uniaxial compression. When the concrete material starts to yield, the stress state can be described by the following equations:

$$\sigma_1 = \sigma_2 = 0; \sigma_3 = -\sigma_c \quad (13)$$

$$p = \frac{1}{3}\sigma_c; q = \sigma_c \quad (14)$$

$$\theta = 0^\circ \quad (15)$$

The mechanical state can satisfy all the four yield conditions listed in Table 7. However, it is evident that the von Mises model ignores the influence of the hydrostatic pressure p, while the 3D printed cementitious materials are mostly brittle materials, the failure of which is sensitive to hydrostatic pressure. By contrast, in the Mohr-Coulomb and Drucker-Prager models, the hydrostatic pressure p is incorporated by applying trigonometric functions of the internal angle ϕ. Meanwhile, the CDP model integrates hydrostatic pressure p using a coefficient α that considers the increasing strength under biaxial compressive conditions.

Regarding flow rules, the von Mises model adopts the associated flow rule and the dilation angle ψ is determined by the yield function: $\psi = tan^{-1}\left(\frac{dq}{dp}\right) = 0^\circ$. This means the plastic volume strain is zero, and plastic volume expansion is ignored. In contrast, the other three plastic models adopt the non-associated flow rule, enabling the specification of the dilation angle and accounting for plastic volume expansion.

Furthermore, the constitutive relationship of fresh concrete evolves from brittle to ductile (strain softening) behaviours [28,29]. This transition imposes limitations on the applicability of the von Mises criterion, which assumes symmetrical behaviours between pure compression and pure tension, an assumption that holds true for the fresh state [30]. However, this criterion proves inadequate for the hardened state, wherein concrete exhibits notably reduced tensile strength when compared to its compressive strength. In contrast, the other three plastic models offer distinct definitions for tensile behaviours.Consequently, the von Mises model may be unsuitable for predicting the mechanical behaviour of fresh 3D printed concrete.

4.2. Analytical calculations of yield stresses and failure layers

The analytical calculation of yield stresses and failure layers was carried out to investigate the usefulness of various constitutive models in characterizing the mechanical behaviours of fresh 3D printed concrete.

For the Mohr-Coulomb model and Drucker-Prager model, the yield conditions in terms of principal stresses under triaxial compression are employed as given below, respectively,

for the Mohr-Coulomb model:

$$\sigma_1 - \sigma_3 + (\sigma_1 + \sigma_3)\sin\varphi - 2c\cos\varphi = 0 \quad (16)$$

and for the Drucker-Prager model:

$$\sigma_1 - \sigma_3 + \frac{\tan\beta}{2 + \frac{1}{3}\tan\beta}(\sigma_1 + \sigma_3) - \frac{1 - \frac{1}{3}\tan\beta}{1 + \frac{1}{6}\tan\beta}\sigma_c^0 = 0 \quad (17)$$

As the uniaxial compression can be seen as a particular situation of triaxial compression, where $\sigma_1 = 0$, Eqs. (16) and (17) are converted as:

for the Mohr-Coulomb model:

$$(\sin\varphi - 1)\sigma_3 - 2c\cos\varphi = 0 \quad (18)$$

and for the Drucker-Prager model:

$$\left(\frac{\tan\beta}{2 + \frac{1}{3}\tan\beta} - 1\right)\sigma_3 - \frac{1 - \frac{1}{3}\tan\beta}{1 + \frac{1}{6}\tan\beta}\sigma_c^0 = 0 \quad (19)$$

Considering the conversion relationship between the Mohr-Coulomb model and Drucker-Prager model, given as below,

$$\tan\beta = \frac{6\sin\varphi}{3 - \sin\varphi} \quad (20)$$

$$\sigma_c^0 = 2c\frac{\cos\varphi}{1 - \sin\varphi} \quad (21)$$

Eqs. (18) and (19) can be merged as one equation below:

Table 7
Yield conditions of various constitutive models.

Models	Yield conditions
von Mises	$f = q - \sigma_c = 0$
Mohr-Coulomb	$f = \left(\frac{1}{\sqrt{3}\cos\phi}\sin\left(\frac{2\pi}{3} - \theta\right) + \frac{1}{3}\tan\phi\cos\left(\frac{2\pi}{3} - \theta\right)\right)q - p\tan\phi - \frac{1 - \sin\phi}{2\cos\phi}\sigma_c = 0$
Drucker-Prager	$f = q - p\frac{6\sin\phi}{3 - \sin\phi} - \left(1 - \frac{2\sin\phi}{3 - \sin\phi}\right)\sigma_c = 0$
Concrete Damage Plasticity	$\sigma_1 \leq 0 : f = q - 3\alpha p + \gamma\sigma_1 - (1-\alpha)\sigma_c = 0 \sigma_1 > 0 : f = q - 3\alpha p + \beta\sigma_1 - (1-\alpha)\sigma_c = 0$

$$\sigma_3 = \frac{2c\cos\varphi}{\sin\varphi - 1} \tag{22}$$

When it comes to the CDP model, in Eq. (8), $\hat{\bar{\sigma}}_{max} = \sigma_1 = \sigma_2 = 0$. Therefore, Eq. (8) is rewritten as:

$$F = \frac{1}{1-\alpha}(\bar{q} - 3\alpha\bar{p}) - \bar{\sigma}_c\left(\tilde{\varepsilon}_c^{pl}\right) = 0 \tag{23}$$

Substituting Eq. (14) into Eq. (23), we obtain

$$\sigma_3 = -\bar{\sigma}_c\left(\tilde{\varepsilon}_c^{pl}\right) \tag{24}$$

According to Eq. (9), the effective compressive cohesion stress $\bar{\sigma}_c\left(\tilde{\varepsilon}_c^{pl}\right)$ can be considered as the critical stress before the concrete material becomes plastic and damaged under uniaxial compression loading.

Therefore, for the Mohr-Coulomb model and Drucker-Prager model, according to Eq. (22), the yield stresses can be derived based on the cohesion stress c and internal friction angle φ. For the CDP model, according to Eq. (24), the yield stress depends on the effective compressive cohesion stress $\bar{\sigma}_c\left(\tilde{\varepsilon}_c^{pl}\right)$.

The values of key material parameters used in four plastic constitutive models are given in Table 8. Since these values are significant to the accuracy of analytical and FE models, the specific derivations of crucial values are given and discussed in Section 4.3.

By substituting the values of material properties from Table 8, including dilation angle φ, cohesion yield stress c and effective compressive cohesion stress $\bar{\sigma}_c\left(\tilde{\varepsilon}_c^{pl}\right)$, into Eqs. (22) and (24), the analytical yield stresses of concrete material using various constitutive models are derived. Table 9 compares the numerical failure stresses of two FE models and analytical failure stresses of concrete using various constitutive models. It can be found that the analytical yield stresses derived by the Mohr-Coulomb model and Drucker-Prager model are identical due to the consistency of their formulations. For wall 1, the stress when elastic buckling occurs, 1.75 kPa, is much lower than all analytical yield stresses derived by different models. This means that the choice of plastic constitutive model is not critical for predicting elastic buckling as the elastic buckling happens before the material yield.

As for Ring 2, it can be found that the analytical yield stresses of different constitutive models, 1.71 and 1.73 kPa, are close to each other and about 16% higher than the numerical results, 1.48 kPa. Furthermore, the analytical results of material yield stresses are converted to the failure layers of 3D printed concrete structures according to the proportional relationship between the failure stress and failure layer, as shown in Table 10. The analytically predicted failure layer, the 13th layer, is also about 16% higher than the numerical and experimental results of the 10th and 11th layers. The main reason for the discrepancies in yield stresses and failure layers between analytical and experimental results may be that the analytical models use idealised assumptions and cannot consider specific conditions of experiments, such as the geometry of the 3D printed concrete structure, which influences the stress distribution and even causes stress concentrations. Another reason could be the adopting value of friction angle from the literature [15], and its exact value should be obtained via experimental testing. Despite this, the consistency of analytical results using different constitutive models and the slight discrepancy from the experimental value prove that the four analytical models can be used to estimate the failure layer of 3D printed concrete structures failing in plastic collapse preliminarily.

Table 8
The values of key material parameters of four constitutive models [13,15].

Models	Parameters	Wall 1	Ring 2
von Mises	Yield stress (kPa)	5.75	1.71
M−C	Cohesion yield stress (kPa)	3.77	0.39
	Friction angle (°)	20	42
	Dilation angle (°)	13	0.7
D-P	Compressive yield stress (kPa)	5.75	1.71
	Angle of friction (°)	37	59
	Dilation angle (°)	13	0.7
	Flow stress ratio	0.778	0.778
CDP	Compressive yield stress (kPa)	5.75	1.71
	Dilation angle (°)	13	0.7
	Eccentricity	0.1	0.1
	f_{b0}/f_{c0}	1.16	1.16
	K	0.6667	0.6667
	Viscosity parameter	0.00001	0.00001

Table 9
The failure stresses derived by numerical simulations and analytical calculations.

Model	Critical stress	von Mises	M-C	D-P	CDP
Wall 1	Yield stress of concrete material (kPa)	5.75	7.95	7.95	5.75
	Stress when elastic bulking occurs (kPa)	1.75			
Ring 2	Yield stress of concrete material (kPa)	1.71	1.73	1.73	1.71
	Stress when plastic collapse occurs (kPa)	1.48			

Table 10
The analytical calculation of failure layers of Ring 2 using various constitutive models.

	von Mises	M-C	D-P	CDP
Analytical results	13	13	13	13
Experimental results	10 and 11			

4.3. Numerical simulations using various constitutive models

To select appropriate constitutive models to characterise the elastic–plastic behaviours of the 3D printed concrete, five constitutive models, including the pure elastic model and four above-mentioned plastic models, were employed in the FE models to predict the failure layers of Ring 2 and Wall 1. The following is the specific derivation of crucial values of various models in Table 8.

The pure elastic model, including two parameters, Young's modulus $E(t)$ and Poisson's ratio ν, was utilized as the control group to analyse the influences of various plastic models on failure behaviours of 3D printed concrete structures. The values of Young's modulus $E(t)$ and Poisson's ratio ν are given in Table 1.

In the von Mises model, the uniaxial yield stress of material should be employed as the input data. In this study, the yield stress of concrete is defined as the critical stress when plastic strain occurs. For Wall 1, according to the strain–stress curve of the triaxial compressive test where the $\sigma_1 = \sigma_2 = 0$ [16], when the stress reached 5.75 kPa, the plastic strain $\varepsilon_p = \varepsilon - \sigma/E$ occurred, which means the concrete yielded. As for Ring 2, however, only direct shear tests were carried out in [15], where the yield stress cannot be obtained. To obtain the yield stress, the FE model of the concrete cylinder using the Mohr-Coulomb model was developed to conduct the uniaxial compressive test. The cylinder dimensions were designed according to the ASTM D2166 [31]. The diameter of $d = 100$ mm is large enough to eliminate the size effect due to particle size and distribution, while the height h is 200 mm so that $h/d = 2$ to allow a diagonal shear failure plane to form, as shown in Fig. 17. The strain–-stress curve of the concrete under the axial loading can be found in Fig. 18 and the yield stress can be determined as 1.71 kPa.

For the Mohr-Coulomb model, the cohesion yield stresses when the failure occurs are adopted instead of using the time-dependent material

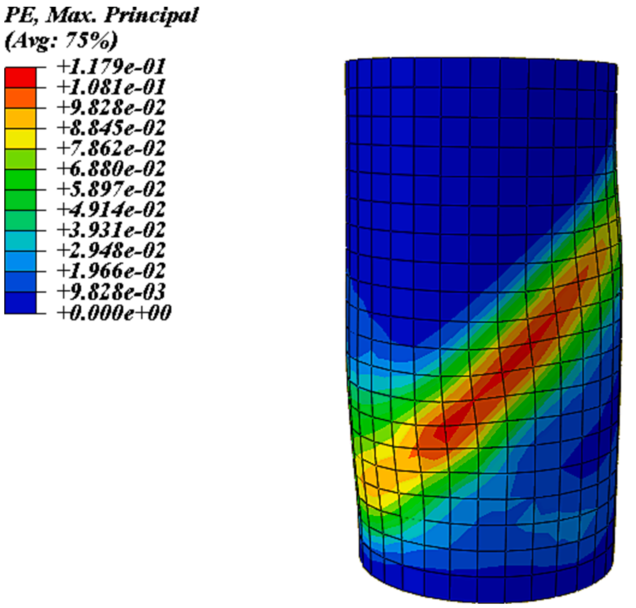

Fig. 17. The diagonal shear failure of concrete cylinder under axial loading.

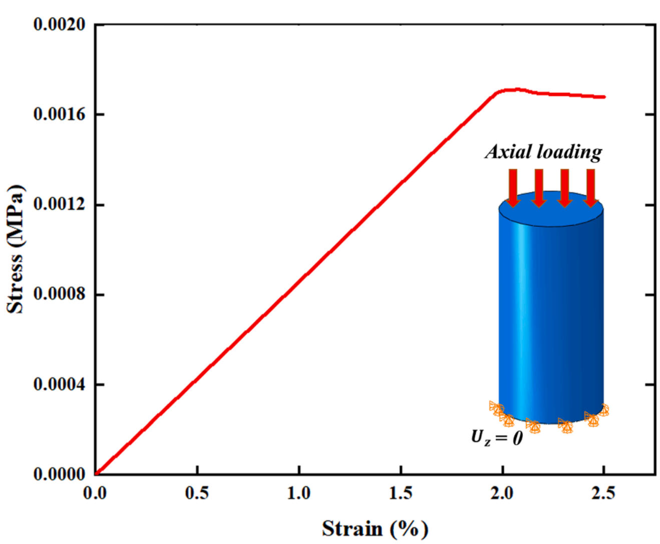

Fig. 18. The strain–stress curve of the concrete in the uniaxial compressive test.

model to control the parameter. The values 3.77 Pa and 0.39 kPa are derived by the time-dependent model of *C(t)* in Table 1. The sensitivity analysis of considering material time-dependence or not was conducted, and the results showed that the difference in failure heights derived from the two methods was within one layer.

In the Drucker-Prager model, the values 5.75 kPa and 1.71 kPa are employed as the compressive yield stresses for Wall 1 and Ring 2, respectively. As for the friction angles and flow stress ratios, they are converted from the data of the Mohr-Coulomb model by Eqs. (20) and (21) as well as $k = \frac{3-\sin\varphi}{3+\sin\varphi}$.

Regarding the CDP model, the compressive yield stresses adopt the same values as those of the Drucker-Prager model. The parameters f_{b0}/f_{co} and K are set as the default values, as they have a few influences on the failure behaviours of 3D printed concrete structures under gravitational loading. A small value of viscosity, e.g., 0.00001, was used to reduce convergence difficulty.

Table 11
The numerically predicted failure layer using various constitutive models.

Model	Pure elasticity	von Mises	M-C	D-P	CDP	Experimental data
Wall 1	23					21 and 22
Ring 2	–	13	11	18	10	10 and 11

Based on the above values of parameters and FE models developed in this study, the numerically predicted failure layers are obtained and given in Table 11. For Wall 1, the numerically predicted failure layer is the 23rd layer regardless of the constitutive model used. Moreover, the contours of plastic strains of Wall 1 using the pure elastic model and Mohr-Coulomb model are shown in Fig. 19. It can be observed that when using the pure elastic constitutive model, the elastic buckling can happen without any plastic strain. However, when using the Mohr-Coulomb model, plastic strains can be seen at the bottom of Wall 1. By comparison, elastic buckling has no relationship with the definition of plastic material properties. Therefore, when the failure height is investigated without considering post-yield behaviour, an excessively detailed definition of material plasticity is a waste for the 3D printed concrete structures that fail in the elastic buckling mode.

Regarding plastic collapse, FE models of Ring 2 with various constitutive models fail at different layers. The numerical results of the Mohr-Coulomb model (the 11th layer) and CDP model (the 10th layer) agree with the experimental results. This means that the two models can simulate the concrete in 3DCP. As for the von Mises model, the failure layer of the 13th layer is higher than the experimental results. This discrepancy may be caused by the reason discussed in Section 4.1. Regarding the Drucker-Prager model, the failure layer of the 18th layer is much higher than the experimental results. This can be attributed to the high friction angle of the concrete used. It is known that in the linear Drucker-Prager model, the value of K should be higher than 0.778 for the yield surface to remain convex, which implies a friction angle $\varphi \leq 22^\circ$. However, the friction angle of the material used in Ring 2 is 59°. In such a case, the approaches to matching Mohr-Coulomb and Drucker-Prager model parameters, including Eqs. (20) and (21), provide poor matching.

5. Conclusions

In this study, some aspects of FE modelling of 3DCP, including additional initial deformations, identification of failure, material model selection, concrete foundation interactions and initial imperfections, have been investigated. Those 3-D FE models using the proposed novel tracing element approach have been developed successfully to simulate layer-by-layer 3DCP processes accurately and then used to investigate failure mechanisms and behaviours of 3D printed concrete structures. The effectiveness of the developed FE models was demonstrated by comparing the obtained numerical results with the data available in literature. Moreover, four constitutive models have been investigated analytically and numerically for their applicability in characterising the early-age mechanical behaviours of 3D printed concrete.

Based on the obtained results, the following conclusions can be drawn.

- The developed FE model using the novel tracing element approach can accurately predict the failure height of 3D printed concrete structures, regardless of whether their failure modes are elastic buckling or plastic collapse.
- The developed tracing element approach can effectively prevent additional initial deformations, improving the accuracy of numerical prediction.
- The mutation of the strains, including logarithmic and plastic strains, of the bottom elements in 3D printed concrete structures can be used as a critical index to identify the structural failure.
- Introducing initial imperfections can obtain more accurate failure-deformation shapes of 3D printed concrete structures failing in elastic buckling.

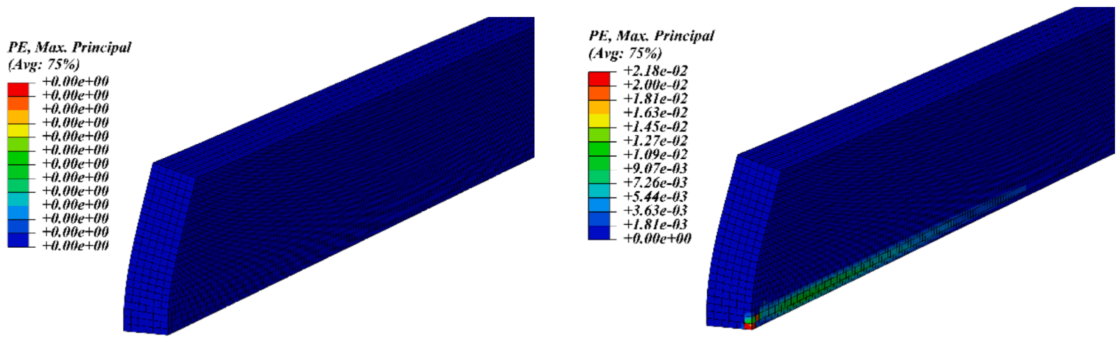

(a) The FE Model using the pure elastic model (b) The FE Model using the Mohr-Coulomb model

Fig. 19. The distributions of plastic strain using the pure elastic model and Mohr-Coulomb model.

- Compared with fixed bottom, rough or frictional interaction can reflect the rheological behaviour of fresh concrete. Strongly constrained boundary condition leads to less displacement, higher stress, and lower failure height.
- Compared with the von Mises model, the Mohr-Coulomb model and CDP model can accurately characterise the mechanical behaviours of 3D printing fresh concrete. The Drucker-Prager model got poor predictions due to its ineffective conversion relationship with the Mohr-Coulomb model when the friction angle exceeds 22°.

Overall, the developed FE models sort out the main technical issues in the numerical simulation of 3DCP and can predict the failure height accurately. However, the proposed FE model cannot reflect the rheological behaviours of the early-age 3D printed concrete. For example, rheological properties, such as yield stresses and viscosity, can be employed to predict the final cross-section shape of the 3D printed concrete layer [32,33]. However, to the author's best knowledge, the mechanical and rheological behaviours have yet to be considered in one model simultaneously due to its complexity. The authors are currently working on the development of a coupled Smooth Particle Hydrodynamics (SPH)/Computational Fluid Dynamics (CFD) - Finite Element Analysis (FEA) analysis process.

CRediT authorship contribution statement

Dong An: Conceptualization, Methodology, Investigation, Writing – original draft, Supervision. **Y.X. Zhang:** Investigation, Visualization, Supervision, Project administration. **Richard (Chunhui) Yang:** Conceptualization, Methodology, Investigation, Visualization, Supervision, Project administration, Funding acquisition.

Declaration of Competing Interest

The authors declare that they have no known competing financial interests or personal relationships that could have appeared to influence the work reported in this paper.

Data availability

Data will be made available on request.

Acknowledgment

The first author acknowledges the PhD scholarship funded by the China Scholarship Council (CSC) and Western Sydney University.

References

[1] Lim S, Buswell RA, Le TT, Austin SA, Gibb AGF, Thorpe T. Developments in construction-scale additive manufacturing processes. Autom Constr 2012;21:262–8.
[2] Bos F, Wolfs R, Ahmed Z, Salet T. Additive manufacturing of concrete in construction: potentials and challenges of 3D concrete printing. Virtual Phys Prototyping 2016;11(3):209–25.
[3] Khan MS, Sanchez F, Zhou H. 3-D printing of concrete: beyond horizons. Cem Concr Res 2020;133.
[4] Mechtcherine V, Nerella VN, Will F, Näther M, Otto J, Krause M. Large-scale digital concrete construction – CONPrint3D concept for on-site, monolithic 3D-printing. Autom Constr 2019;107.
[5] van den Heever M, Bester F, Kruger J, van Zijl G. Mechanical characterisation for numerical simulation of extrusion-based 3D concrete printing. J. Build Eng 2021;44.
[6] Muthukrishnan S, Ramakrishnan S, Sanjayan J. Technologies for improving buildability in 3D concrete printing. Cem Concr Compos 2021;122.
[7] Roussel N. Rheological requirements for printable concretes. Cem Concr Res 2018;112:76–85.
[8] Le TT, Austin SA, Lim S, Buswell RA, Gibb AGF, Thorpe T. Mix design and fresh properties for high-performance printing concrete. Mater Struct 2012;45(8):1221–32.
[9] Bong SH, Xia M, Nematollahi B, Shi C. Ambient temperature cured 'just-add-water' geopolymer for 3D concrete printing applications. Cem Concr Compos 2021;121.
[10] Vantyghem G, Ooms T, De Corte W. VoxelPrint: a Grasshopper plug-in for voxel-based numerical simulation of concrete printing. Autom Constr 2021;122.
[11] Carlo D. Experimental and Numerical Techniques to Characterize Structural Properties of Fresh Concrete Relevant to Contour Crafting. University of Southern California; 2012. Doctoral thesis.
[12] Xiao J, Liu H, Ding T. Finite element analysis on the anisotropic behavior of 3D printed concrete under compression and flexure. Addit Manuf 2021;39.
[13] Wolfs RJM, Bos FP, Salet TAM. Early age mechanical behaviour of 3D printed concrete: Numerical modelling and experimental testing. Cem Concr Res 2018;106:103–16.
[14] Wolfs RJM, Suiker ASJ. Structural failure during extrusion-based 3D printing processes. Int J Adv Manuf Technol 2019;104(1–4):565–84.
[15] Jayathilakage R, Rajeev P, Sanjayan JG. Yield stress criteria to assess the buildability of 3D concrete printing. Constr Build Mater 2020;240.
[16] Wolfs RJM, Bos FP, Salet TAM. Triaxial compression testing on early age concrete for numerical analysis of 3D concrete printing. Cem Concr Compos 2019;104.
[17] Ooms T, Vantyghem G, Van Coile R, De Corte W. A parametric modelling strategy for the numerical simulation of 3D concrete printing with complex geometries. Addit Manuf 2021;38.
[18] Liu X, Sun B. The influence of interface on the structural stability in 3D concrete printing processes. Addit Manuf 2021;48.
[19] Nguyen-Van V, Nguyen-Xuan H, Panda B, Tran P. 3D concrete printing modelling of thin-walled structures. Structures 2022;39:496–511.
[20] Roussel N, Spangenberg J, Wallevik J, Wolfs R. Numerical simulations of concrete processing: from standard formative casting to additive manufacturing. Cem Concr Res 2020;135.
[21] Nguyen-Van V, Panda B, Zhang G, Nguyen-Xuan H, Tran P. Digital design computing and modelling for 3-D concrete printing. Autom Constr 2021;123.
[22] Dassault Syst'emes Simulia Corp, Abaqus User's Manual 2018 (accessed 15 September 2020).
[23] Nerella VN, Krause M, Mechtcherine V. Direct printing test for buildability of 3D-printable concrete considering economic viability. Autom Constr 2020;109.
[24] Ramière I, Angot P, Belliard M. A fictitious domain approach with spread interface for elliptic problems with general boundary conditions. Comput Methods Appl Mech Eng 2007;196(4–6):766–81.

[25] Suiker ASJ. Mechanical performance of wall structures in 3D printing processes: theory, design tools and experiments. Int J Mech Sci 2018;137:145–70.

[26] Famiglietti CM, Prevost JH. Solution of the slump test using a finite deformation elastoplastic Drucker-Prager model. Int J Rock Mech Min Sci Geomech Abs 1995; 32(4):A154–.

[27] Lubliner J, Oliver J, Oller S, Oñate E. A plastic-damage model for concrete. Int J Solids Struct 1989;25(3):299–326.

[28] Esnault V, Labyad A, Chantin M, Toussaint F. Experience in online modification of rheology and strength acquisition of 3D printable mortars. In: First RILEM International Conference on Concrete and Digital Fabrication-Digital Concrete 2018. Springer; 2019. p. 24–38.

[29] Rahul AV, Santhanam M. Evaluating the printability of concretes containing lightweight coarse aggregates. Cem Concr Compos 2020;109.

[30] Ducoulombier N, Mesnil R, Carneau P, Demont L, Bessaies-Bey H, Caron J-F, et al. The "Slugs-test" for extrusion-based additive manufacturing: Protocol, analysis and practical limits. Cem Concr Compos 2021;121.

[31] Standard Test Method for Unconfined Compressive Strength of Cohesive Soil, ASTM D2166.

[32] Reinold J, Nerella VN, Mechtcherine V, Meschke G. Extrusion process simulation and layer shape prediction during 3D-concrete-printing using the Particle Finite Element Method. Autom Constr 2022;136.

[33] Comminal R, Leal da Silva WR, Andersen TJ, Stang H, Spangenberg J. Modelling of 3D concrete printing based on computational fluid dynamics. Cem Concr Res 2020; 138.